RSC Advances

PAPER

View Article Online
View Journal | View Issue

Cite this: *RSC Adv.*, 2022, **12**, 14858

Approaching high performance Ni(Co) molybdate electrode materials for flexible hybrid devices

Yuchen Sun,[a] Xiaowei Wang,[a] Ahmad Umar[b] and Xiang Wu *[a]

Received 19th March 2022
Accepted 29th April 2022

DOI: 10.1039/d2ra01778d

rsc.li/rsc-advances

Transition metal molybdates are widely used as electrode materials for supercapacitors due to their high theoretical specific capacitance and excellent electrochemical activity. It is an effective strategy to improve the electrochemical performance by reasonably designing electrode materials. Herein, we prepared several $Ni_{1-x}Co_xMoO_4 \cdot nH_2O$ nanostructures through facile hydrothermal strategies. Benefiting from the synergistic effects between Ni and Co elements, the obtained electrode materials delivered a specific capacitance of 1390 F g^{-1} at 1 A g^{-1}. The as-assembled device shows an energy density of 72.45 W h kg^{-1} at a power density of 2688.8 W kg^{-1}. It also presents excellent cycling and mechanical stability after many times of charging and discharging processes and bending.

Introduction

At present, the rapid development of portable electronic devices has prompted one to seek for some clean and sustainable energy sources, such as wind energy, hydrogen energy, and solar energy.[1–4] Among various energy storage systems, supercapacitors have been extensively studied because of their high power density, short charging time and superior energy density.[5–9] However, the faradaic redox reaction occurs only on and near the surface of electrode materials, which makes their energy density lower than many rechargeable batteries.[10] This greatly limits their practical application. According to previous reports, one of the strategies to solve this problem is to rationally construct advanced electrode materials with high specific capacitance.[11–14] An important task is to efficiently control the morphology and structures of the active components.

Recently, transition metal oxides have been regarded as promising electrode materials for electrochemical capacitors due to their rich valence states.[15–18] $NiMoO_4$ electrode materials are considered an ideal candidate for supercapacitor cathodes. However, it shows poor cycle stability. In contrast, $CoMoO_4$ electrode materials present excellent rate performance but low charge storage capacity.[19] In general, the co-existence of Ni and Co ions can generate various redox reactions during the reaction process, which is beneficial to improve the electrochemical activity.[20–23] For instance, Zhuo *et al.* synthesized hierarchical $CoMoO_4$–$NiMoO_4$ nanostructures with a specific capacitance of 1079 F g^{-1} at 5 A g^{-1}.[24] Similarly, $NiMoO_4$@$CoMoO_4$ nanospheres can be obtained through adjusting the proportion of $NiMoO_4$ and $CoMoO_4$. It delivers a specific capacitance of 1601.6 F g^{-1} at 2 A g^{-1}.[25]

Herein, we synthesized several hydrous $Ni_{1-x}Co_xMoO_4 \cdot nH_2O$ products through a facile hydrothermal approach. By tailoring the Ni/Co ratio, it is found that when Ni : Co = 3 : 1, the composite materials deliver excellent specific capacitance compared to others. In addition, we assembled an asymmetric supercapacitor (ASC) using the as-synthesized sample as a positive electrode material. As expected, the maximum energy density is 72.45 W h kg^{-1} at 2688.8 W kg^{-1}. The device retains 94.4% of initial capacity after 11 000 cycles, demonstrating its excellent cycling stability.

Experimental section

All reagents are analytically pure without further purification. In a typical procedure, a piece of 3 × 3 cm^2 nickel foam (NF) was immersed into 1 M HCl solution and sonicated for 30 min. Next, the NF was repeatedly washed with ethanol and deionized water, respectively, and then dried overnight.

Synthesis of $Ni_xCo_{1-x}MoO_4 \cdot nH_2O$ samples

A $Ni_xCo_{1-x}MoO_4 \cdot nH_2O$ hybrid structure was prepared by a one-step hydrothermal approach. In detail, $Ni(NO_3)_2 \cdot 6H_2O$, $Co(NO_3)_2 \cdot 6H_2O$ and $Na_2MoO_4 \cdot 2H_2O$ were in turn dissolved into 50 mL deionized water with different molar ratios (Table 1). After magnetic stirring for 0.5 h, a clean NF was put into a reaction kettle and heated at 150 °C for 6 h. Then, the precursors are taken out and annealed to obtain different Ni/Co molybdates. The detailed annealing parameters were kept at 350 °C for 2 h at 2 °C min. Their load masses are 1.8, 1.2, 1, 1.6, 1.4 mg cm^{-2}, respectively. The corresponding products were denoted as NMOH, NCMOH-1, NCMOH-2, NCMOH-3 and CMO.

[a]School of Materials Science and Engineering, Shenyang University of Technology, Shenyang 110870, P. R. China. E-mail: wuxiang05@163.com; wuxiang05@sut.edu.cn
[b]Department of Chemistry, College of Science and Arts, Najran University, Najran 11001, Saudi Arabia

Table 1 Reagent dosage ratio and load mass of electrode materials

Labels	$Ni(NO_3)_2 \cdot 6H_2O$	$Co(NO_3)_2 \cdot 6H_2O$	$Na_2MoO_4 \cdot 2H_2O$	Molar ratios
NMOH	2	0	2	1 : 0
NCMOH-1	0.5	1.5	2	1 : 3
NCMOH-2	1	1	2	1 : 1
NCMOH-3	1.5	0.5	2	3 : 1
CMO	0	2	2	0 : 1

Structural characterizations

The morphology of the as-synthesized $Ni_xCo_{1-x}MoO_4 \cdot nH_2O$ materials was characterized by scanning electron microscopy (SEM) and transmission electron microscopy (TEM), respectively. The crystal structure and element distribution were confirmed by X-ray powder diffraction (XRD, Shimadzu-7000) and X-ray photoelectron spectrum (XPS) measurements (ESCALAB250, Themo VG) with an Al Kα source. The electrochemical measurements were performed in a 3 M KOH solution on a CHI660E electrochemical workstation with a three-electrode system. The as-prepared electrode, Pt foil and Hg/HgO electrode (+0.098 V *vs.* SHE) were used as the working electrode, counter electrode and reference electrode, respectively. The electrochemical tests include cyclic voltammetry (CV), galvanostatic charge–discharge (GCD) and electrochemical impedance spectroscopy (EIS). The mass specific capacitance (C_s), energy density (E) and power density (P) are calculated by the following equations:

$$C_s = I \times \Delta t/m \quad (1)$$

$$E = 1/2 \times C \times V^2 \quad (2)$$

$$P = 3600 \times E/\Delta t \quad (3)$$

where I, Δt, and V are the current density (A g^{-1}), discharge time (s) and potential window (V), respectively.

Assembly of hybrid supercapacitor

Finally, the negative electrode was obtained by coating a nickel foam with a slurry of activated carbon (70 wt%), carbon black (20 wt%) and PVDF (10 wt%) and dried at 80 °C for 24 h. An asymmetric device was assembled with the NCMOH-1 sample as positive materials, active carbon as negative ones and PVA-KOH gel as an electrolyte. In order to balance the charges between positive and negative electrodes, the following formulae were used:[26]

$$Q = It = Cm\Delta V \quad (4)$$

$$m^+/m^- = C_m{}^-\Delta V^-/C_m{}^+\Delta V^+ \quad (5)$$

In above formula, $C_m{}^+$ and $C_m{}^-$ represent the specific capacitance of the positive and negative electrodes (F g^{-1}), respectively. m^+ and m^- stand for the mass loading of the positive and negative electrodes (mg), respectively. Q is the electric quantity. ΔV^+ and ΔV^- denote the voltage windows of the positive and negative electrode (V), respectively. The mass loading of NCMOH-1 and AC on the Ni foam was optimized to be around 1.5 and 2.5 mg cm^{-2}, respectively.

Results and discussion

First, we studied the crystal structure and phase purity of the obtained samples by XRD. From Fig. 1a, the diffraction peaks of the CMO sample correspond to the $CoMoO_4$ crystal structure (PDF#21-0868), and there are no miscellaneous peaks, revealing its good crystallinity. Similarly, the main diffraction peaks of NMOH samples can be indexed to the triclinic $NiMoO_4 \cdot nH_2O$ phase (PDF# 13-0128).[27] Also, the (001) and (312) crystal plane belongs to the $NiMoO_4$ phase (PDF# 45-0142). From Fig. 1b, after a small amount of Co atoms was substituted by Ni atoms, the lattice parameters of $NiMoO_4$ remain unchanged. As the Co content increases, the strong diffraction peak of the $NiMoO_4$ structure at 29.8° gradually weakens and disappears. Moreover, the main diffraction peak of the $CoMoO_4$ structure appears at 26.5°. It can be clearly observed that the (201), (112), (311) and (131) crystal planes of the $CoMoO_4$ phase appear when the ratio of Ni : Co is 1 : 1. This may be due to the partial phase change from $NiMoO_4$ to $CoMoO_4$ during the process of Co gradually replacing Ni ions.

XPS spectroscopy is employed to investigate the surface chemical compositions of the as-synthesized NCMOH-1 electrode. Co 2p spectra (Fig. 1c) consists of two spin doublets located at 780.0 eV and 795.5 eV, which can be indexed to Co^{3+} species, while those at 782.1 eV and 798.7 eV correspond to Co^{2+} species. The presence of the satellite peaks further proves the co-existence of Co^{2+} and Co^{3+} in the obtained NCMOH-1 structure.[28] Ni 2p spectra are shown in Fig. 1d. Two main peaks at 856.5 and 874.2 eV correspond to Ni $2p_{3/2}$ and Ni $2p_{1/2}$, suggesting the existence of a Ni^{2+} oxidation state.[29] From Fig. 1e, Mo 3d high-resolution spectra also show two characteristic peaks of Mo $3d_{3/2}$ and Mo $3d_{5/2}$ at 231.9 eV and 235.1 eV, indicating Mo^{6+} with a high oxidation state.[30] Furthermore, Fig. 1f shows the O 1s spectra. O1 (533.2 eV), O2 (531.6 eV), and O3 (533.2 eV) peaks represent metal–oxygen bonds, defective oxygen, and OH groups from surface-adsorbed moisture, respectively.[31]

The morphology and structure of the as-prepared samples are then characterized by SEM and TEM, respectively. Fig. 2a shows that the NMOH nanorods with the average diameter of about 10–50 nm are homogeneously grown on NF. From Fig. 2b and f, when Ni/Co = 3 : 1, the Co ion concentration is so low that the NCMOH-1 sample still shows one-dimensional nanorods. In addition, it can be clearly seen that the average

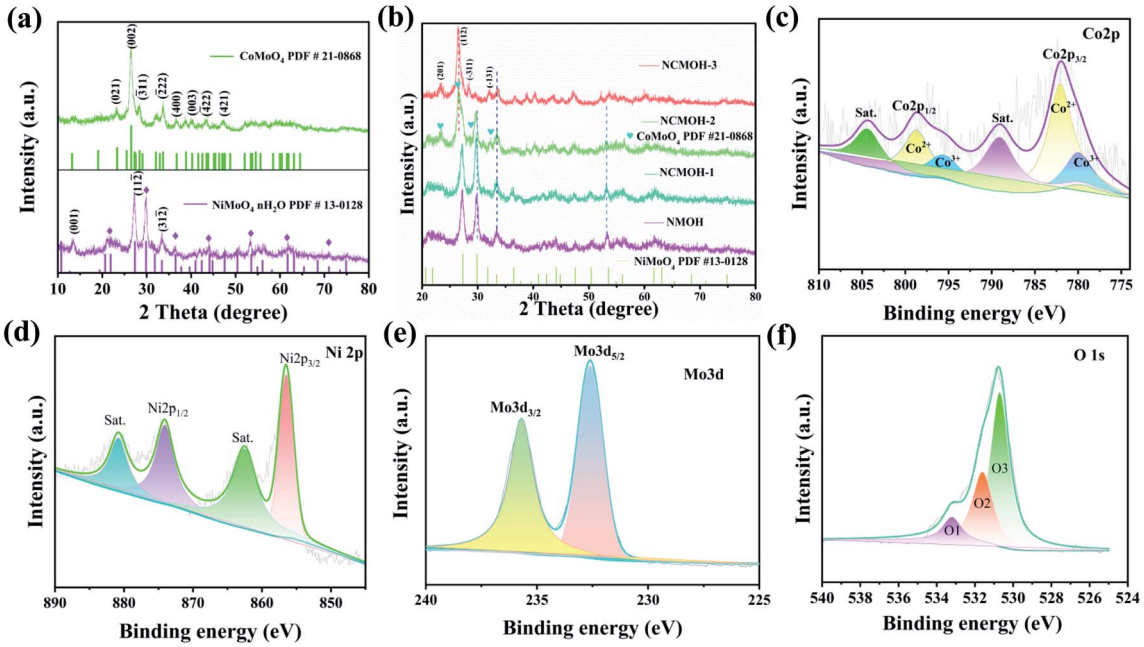

Fig. 1 Structural characterization of the as-prepared samples (a and b) XRD patterns (c–f) XPS spectra of the NCMOH-1 sample.

diameter of NCMOH-1 increases. When the Ni/Co molar ratio is 1 : 1, the morphology of the sample becomes a $CoMoO_4$ sheet-like structure (Fig. 2c and g). As shown in Fig. 2d and h, numerous sheets are the interconnected network structure. The morphology of CMO product is shown in Fig. 2e when Ni atoms are completely replaced by Co atoms. It is completely transformed into a uniform nanosheet network structure. The low magnification TEM image of the NCMOH-1 sample in Fig. 3a shows a layered structure composed of numerous nanorods, which is in good agreement with the SEM result. The corresponding HRTEM (Fig. 3b) indicates that the d-spacing value of 0.82 nm belongs to the $NiMoO_4 \cdot nH_2O$ crystal phase. In Fig. 2c, the lattice spacing of 0.32 nm corresponds well to the (202) crystal plane of the $CoMoO_4$ structure, indicating that the

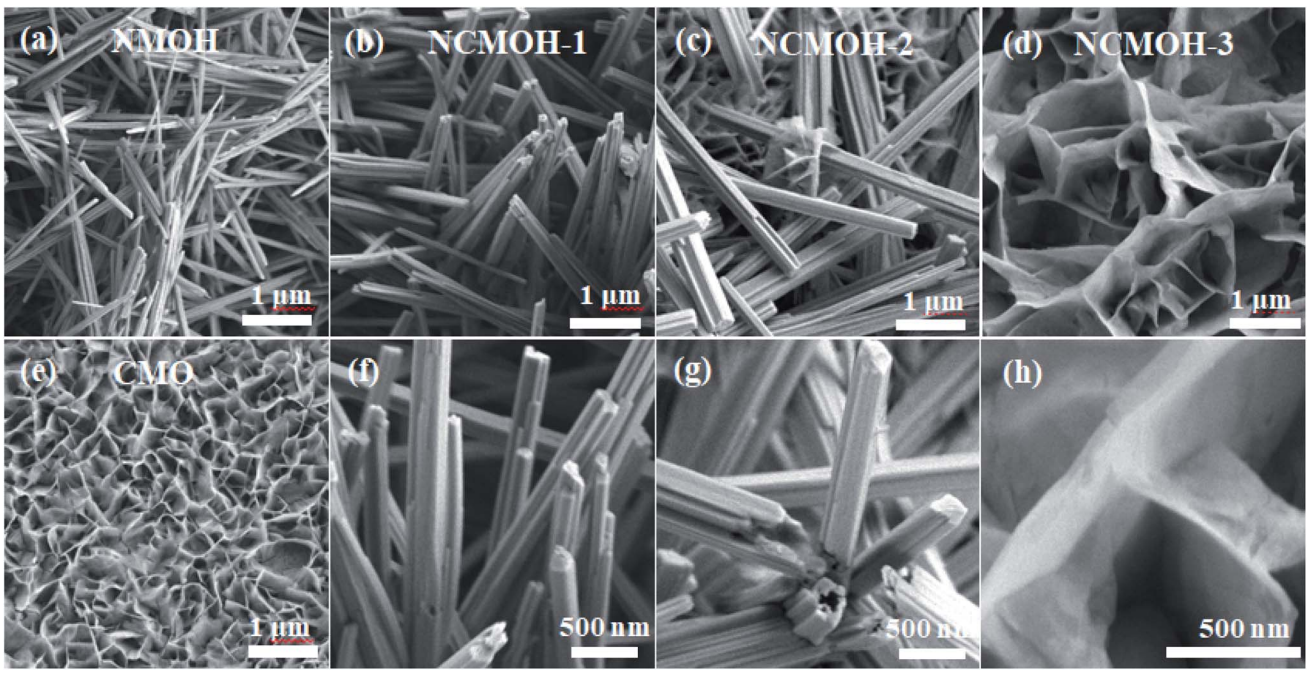

Fig. 2 Low and high magnification SEM images of the as-prepared samples. (a) NMOH nanorods, (b) and (f) NCMOH-1, (c) and (g) NCMOH-2, (d) and (h) NCMOH-3, and (e) CMO nanosheets.

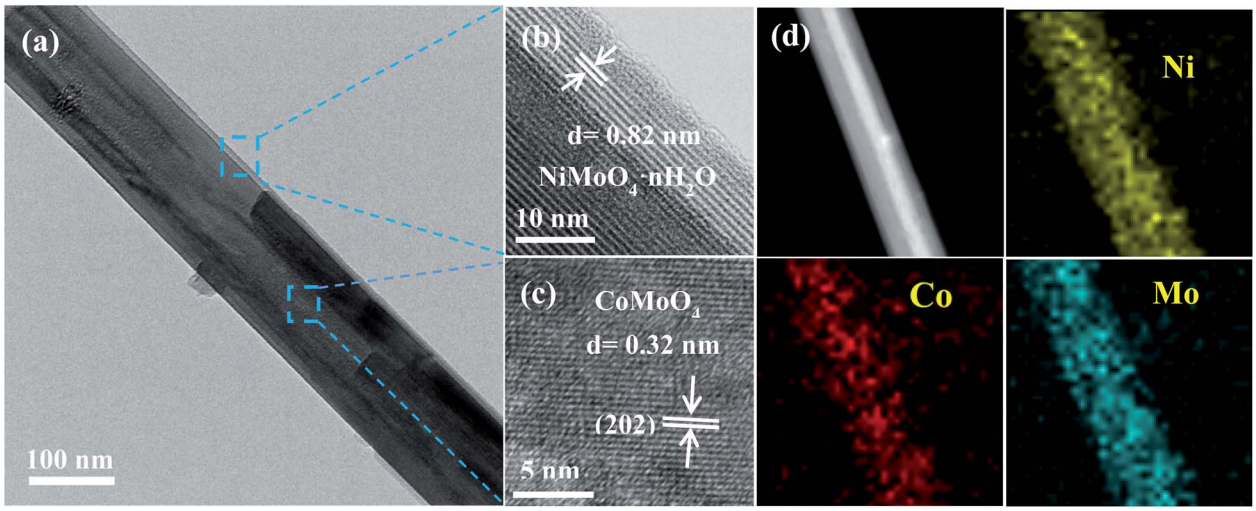

Fig. 3 (a) TEM and (b and c) HRTEM images of the NCMOH-1 product. (d) HAADF-STEM image with the line–scan profiles across a single nanorod and the corresponding EDS element mappings.

NCMOH-1 sample has been successfully prepared. As shown in Fig. 3d, the elemental mapping images further prove that the elements of Ni, Co, Mo and O are well coated on the surface of NCMOH-1 nanorods.

Then, we studied the electrochemical performance of different samples in a 3 M KOH electrolyte. Fig. 4a presents the CV curves of several electrode materials at 10 mV s^{-1}. Evidently, the NCMOH-1 material shows the largest integral area, indicating excellent specific capacitance. Moreover, a pair of obvious redox peaks represents a typical faradaic behavior of electrode materials.[29] The redox process of electrode materials in an electrolyte can be described by the following formulas:[32]

$$Ni(OH)_2 + OH^- \leftrightarrow NiOOH + H_2O + e^- \quad (6)$$

$$Co(OH)_2 + OH^- \leftrightarrow CoOOH + H_2O + e^- \quad (7)$$

$$CoOOH + OH^- \leftrightarrow CoO_2 + H_2O + e^- \quad (8)$$

As shown in Fig. 4b, the GCD curves of the samples indicate obvious charge–discharge platforms, which further confirm the occurrence of a faradaic redox reaction. Among them, the NCMOH-1 electrode delivers a specific capacitance of 695C g^{-1} at 1 A g^{-1}. It is superior to some previous reports (Table 2).[33–38]

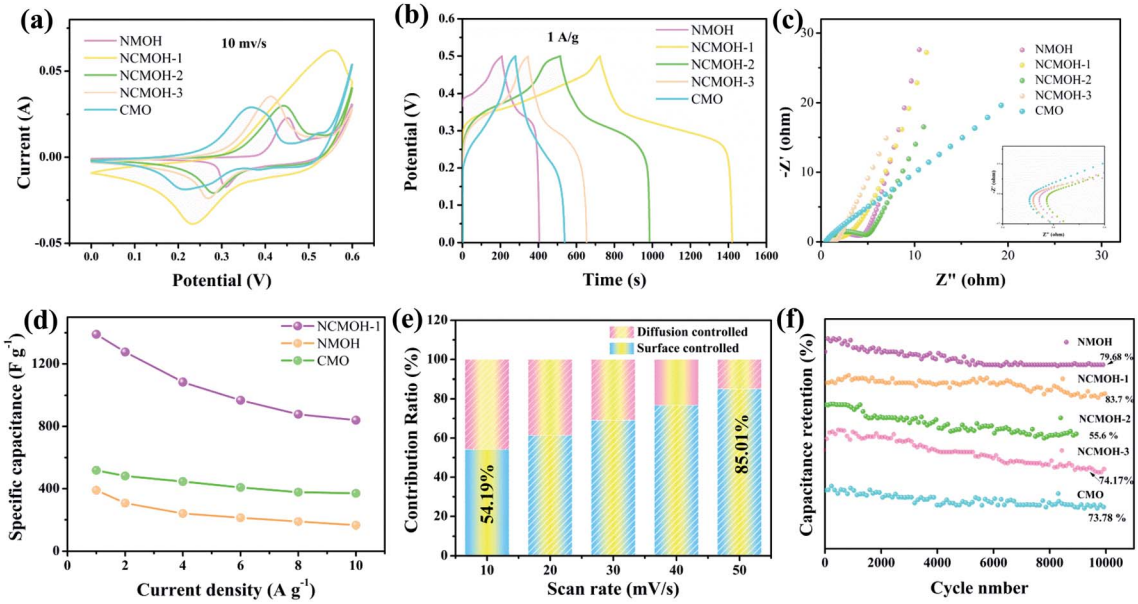

Fig. 4 Electrochemical performance of the electrode materials. (a) CV curves at 10 mV s^{-1}, (b) GCD curves at 1 A g^{-1}, (c) Nyquist plots of the electrode materials, (d) specific capacitance values of the samples, (e) the normalized contribution ratio with capacitive and diffusion contribution at different scan rates, and (f) cycling stability.

Table 2 Electrochemical performance of various electrode materials

Electrode materials	Capacitance (F g^{-1})	Current density (A g −1)	Electrolyte	Ref.
$NiMoO_4 \cdot H_2O$ nanoclusters	680	1	6 M KOH	33
$CoMoO_4$ nanoparticles	771.6	1	2 M KOH	34
$NiMoO_4$@$CoMoO_4$ hollow nanorods	1329	0.5	6 M KOH	35
$NiMoO_4$ nanorods	594	1	6 M KOH	36
$NiMoO_4$/$CoMoO_4$ clusters	740	1	3 M KOH	37
Co–Mo–S nanosheets	1020	1	3 M KOH	38
NCMOH-1 nanorods	1400	1	3 M KOH	This work

EIS was further used to investigate the electrochemical performance of electrode materials in the frequency range from 100 kHz to 0.01 Hz. The corresponding Nyquist plots are shown in Fig. 4c. The straight line in a low frequency zone refers to the diffusive resistance of electrolyte ions (R_w). It is associated with the diffusivity of electrolyte ions within electroactive materials.[39] In a high frequency region, the intersection with the real axis refers to bulk resistance (R_s) and the diameter of semicircle represents the charge transfer resistance (R_{ct}). The R_s value of NCMOH-1 is 0.52 Ω, which is lower than those of the others.

Fig. 4d shows the specific capacitance of several electrode materials at different current densities. It indicates that the specific capacitance of the NCMOH-1 sample is twice that of single electrode materials at 1 A g^{-1}. It keeps a high specific capacitance even at large current density, demonstrating its excellent rate performance. As is known, the charge storage of

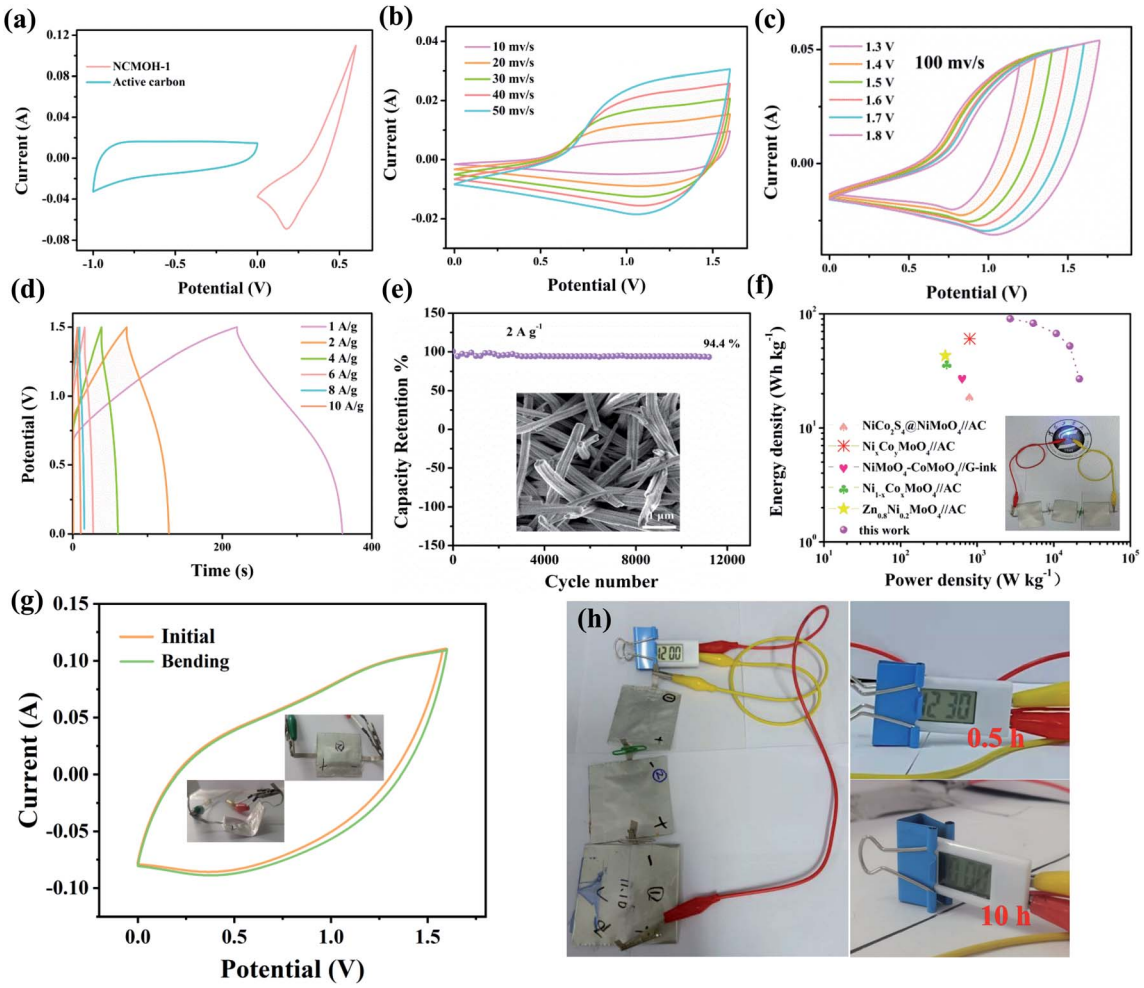

Fig. 5 (a) CV curves of the electrodes at 100 mV s^{-1}, (b) CV curves at different scanning rates, (c) CV curves at different voltages, (d) GCD curves, (e) cycling performance of the device, (f) Ragone plot, (g) capacitance retention after bending, and (h) digital photo of an electronic clock by 3 devices in series.

electrode materials consists of two different electrochemical processes, including surface-controlled process and diffusion-controlled one. To further explore the electrochemical reaction kinetics of the electrode materials, capacitive contribution can be calculated according to the following equation:[39]

$$i = av^b \quad (9)$$

b values are used to judge whether the as-prepared product has pseudocapacitive behavior during charging and discharging processes.

The capacitive contribution ratio can be further quantified by the equation:

$$i = k_1 v + k_2 v^{1/2} \quad (10)$$

where i, v, k_1 and k_2 are the measured current, scan rate, and constants, respectively. The calculated capacitive contribution at different scan rates is shown in Fig. 4e. It can be found that the increase in the scan rate is inversely proportional to the contribution of diffusion-controlled capacitance. It indicates that the optimized ratio is favorable for the rapid penetration of OH^- on the electrode surface.[19] Apart from specific capacitance, cyclic stability is a crucial factor for evaluating the performance of electrode materials. Fig. 4f is the capacitance curves of the electrode materials after 10 000 cycles of charge–discharge at 10 A g^{-1}. The NMOH-1 electrode material still retains 83.7% of its initial capacitance after 10 000 cycles, confirming its excellent durability.

To explore the potential application of electrode materials, several supercapacitors were assembled. The NCMOH-1 product, activated carbon, and KOH gel were used as the positive electrode, negative electrode, and electrolyte, respectively, to form a sandwich structure. As shown in Fig. 5a, the positive and negative materials are well matched, and the operating voltage of the device reached 1.6 V. Fig. 5b shows the CV curves of the device at different scan rates. All CV curves present almost similar shapes as the scan rate increases, indicating that they possess good capacitive performance. The CV curve tests at different voltage windows are conducted to study the suitable voltage range of the device (Fig. 5c). It shows that the device can operate stably at 1.6 V without any obvious polarization phenomenon. The electrochemical behavior was further investigated by GCD tests (Fig. 5d). It can be found that the curves are nearly symmetric, revealing the ideal battery-type behavior and rate capability. Moreover, the capacitance of the device only reduces 5.6% after 10 000 cycles (Fig. 5e), indicating its excellent durability. The inset in Fig. 5e shows that the NCMOH-1 material retains its original morphology after multiple charge–discharge processes. The Ragone plot (Fig. 5f) lists the energy and power density of some supercapacitors. The NCMOH-1//AC device delivers a maximum energy density of 72.45 W h kg^{-1} at a power density of 2688.8 W kg^{-1}, which is higher than those of the previously reported works.[40–44] The inset shows a blue LED powered by 3 devices in series (the voltage window is about 2.8 V).

Finally, we studied the effects of folds on the electrochemical behavior of the assembled device. Fig. 5g shows that the shape of CV curves almost does not change after bending, indicating its excellent mechanical stability. This may be attributed to the three-dimensionally porous structure of the electrode materials. In addition, three devices in series were used to power an electronic clock for more than 10 h, as shown in Fig. 5h. It suggests that the prepared electrode materials can be used in future portable flexible electronic devices.

Conclusions

In summary, we have synthesized several nickel/cobalt mixed molybdates with different Ni/Co molar ratios through a simple hydrothermal strategy. The as-prepared NCMOH-1 (Ni/Co = 3 : 1) sample demonstrates superior electrochemical performance than single metal molybdates such as NMOH and CMO electrodes. The results show that the synergistic effect of Ni and Co ions can improve the specific capacitance and rate performance of electrode materials, while Co ions can enhance the cycling stability. Therefore, it is feasible to design multi-component electrode materials to improve their electrochemical performance. The assembled asymmetric capacitors can drive small electronic equipment and show excellent mechanical stability.

Conflicts of interest

There are no conflicts to declare.

References

1 Y. Liu and X. Wu, *J. Energy Chem.*, 2021, **56**, 223–237.
2 X. Y. Li, R. F. Zhou, Z. Z. Wang, M. H. Zhang and T. S. He, *J. Mater. Chem. A*, 2022, **10**, 1642–1681.
3 M. Z. Dai, F. D. P. Zhao and X. Wu, *Chin. Chem. Lett.*, 2020, **31**, 2177–2188.
4 Y. Liu, P. F. Hu, H. Q. Liu, X. Wu and C. Y. Zhi, *Mater. Today Energy*, 2020, **17**, 100431.
5 X. Y. Li, L. Zhao, T. S. He, M. H. Zhang, Z. Z. Wang, B. Zhang and X. Weng, *J. Power Sources*, 2022, **521**, 230943.
6 D. P. Zhao, M. Z. Dai, H. Q. Liu, Z. X. Duan, X. J. Tan and X. Wu, *J. Energy Chem.*, 2022, **69**, 292–300.
7 Y. Gogotsi and P. Simon, *Science*, 2011, **334**, 917–918.
8 M. D. Wang, X. Y. Liu, H. Q. Liu, D. P. Zhao and X. Wu, *J. Alloys Compd.*, 2022, **903**, 163926.
9 A. M. Zardkhoshoui and S. S. H. Davarani, *Chem. Eng. J.*, 2020, **402**, 126241.
10 H. Q. Liu, D. P. Zhao, P. F. Hu, K. F. Chen, X. Wu and D. F. Xue, *Mater. Today Phys.*, 2020, **13**, 100197.
11 C. Q. Teng, X. H. Gao, N. Zhang, Y. Jia, X. Y. Li, Z. Y. Shi, Z. X. Wu, M. J. Zhi and Z. L. Hong, *RSC Adv.*, 2018, **8**, 32979–32984.
12 Z. N. Yu, L. Tetard, L. Zhai and J. Thomas, *Energy Environ. Sci.*, 2015, **8**, 702–730.
13 C. Jing, B. Q. Dong and Y. X. Zhang, *Energy Environ. Mater.*, 2020, **3**, 346–379.
14 Y. Liu, D. P. Zhao, H. Q. Liu, A. Umar and X. Wu, *Chin. Chem. Lett.*, 2019, **30**, 1071–1076.

15 H. W. Lai, Q. Wu, J. Zhao, L. M. Shang, H. Li, R. C. Che, Z. Lyu, J. Xiong, L. Yang, X. Wang and Z. Hu, *Energy Environ. Sci.*, 2016, **9**, 2053–2060.
16 T. Xia, D. P. Zhao, Q. Xia, A. Umar and X. Wu, *RSC Adv.*, 2021, **11**, 39045–39050.
17 V. Augustyn, P. Simon and B. Dunn, *Energy Environ. Sci.*, 2014, **7**, 1597–1614.
18 Y. Zhao, J. F. He, M. Z. Dai, D. P. Zhao, X. Wu and B. D. Liu, *J. Energy Chem.*, 2020, **45**, 67–73.
19 H. C. Chen, S. Chen, Y. Y. Zhu, C. Li, M. Q. Fan, D. Chen, G. L. Tian and K. Y. Shu, *Electrochim. Acta*, 2016, **190**, 57–63.
20 X. W. Wang, Y. C. Sun, W. C. Zhang, J. Liu and X. Wu, *Mater. Today Sustain.*, 2022, **17**, 100097.
21 C. Liu, X. Wu and H. Xia, *CrystEngComm*, 2018, **20**, 4735–4744.
22 F. Nti, D. A. Anang and J. I. Han, *J. Alloys Compd.*, 2018, **742**, 342–350.
23 T. Xia, Y. Liu, M. Z. Dai, Q. Xia and X. Wu, *Dalton Trans.*, 2021, **50**, 4045–4052.
24 Z. X. Yin, Y. J. Chen, Y. Zhao, C. Y. Li, C. L. Zhu and X. T. Zhang, *J. Mater. Chem. A*, 2015, **3**, 22750–22758.
25 Z. Zhang, Y. D. Liu, Z. Y. Huang, L. Ren, X. Qi, X. L. Wei and J. X. Zhong, *Phys. Chem. Chem. Phys.*, 2015, **17**, 20795–20804.
26 Y. L. Tong and X. Wu, *Energy Storage Sci. Technol.*, 2022, **11**, 1035–1043.
27 K. Eda, Y. Kato, Y. Ohshiro, T. Sugitani and M. S. Whittingham, *J. Solid State Chem.*, 2010, **183**, 1334–1339.
28 Y. H. Zhao, X. Y. He, R. R. Chen, Q. Liu, J. Y. Liu, D. L. Song, H. S. Zhang, H. X. Dong, R. M. Li, M. L. Zhang and J. Wang, *Appl. Surf. Sci.*, 2018, **453**, 73–82.
29 X. Y. Zhang, Z. Li, Z. Y. Yu, L. Wei and X. Guo, *Appl. Surf. Sci.*, 2020, **505**, 144513.
30 M. J. Pang, S. Jiang, Y. Ji, J. G. Zhao, B. Y. Xing, Q. L. Pan, H. Yang, W. S. Qu, L. Gu and H. Q. Wang, *J. Alloys Compd.*, 2017, **708**, 14–22.
31 C. Qing, C. X. Yang, M. Y. Chen, W. H. Li, S. Y. Wang and Y. W. Tang, *Chem. Eng. J.*, 2018, **354**, 182–190.
32 Y. Q. Guo, X. F. Hong, Y. Wang, Q. Li, J. S. Meng, R. T. Dai, X. Liu, L. He and L. Q. Mai, *Adv. Funct. Mater.*, 2019, **29**, 1809004.
33 H. Z. Wan, J. J. Jiang, X. Ji, L. Miao, L. Zhang, K. Xu, H. C. Chen and Y. J. Ruan, *Mater. Lett.*, 2013, **108**, 164–167.
34 R. M. Bhattarai, S. M. S. Pandiyarajan, S. Saud, S. J. Kim and Y. S. Mok, *Dalton Trans.*, 2020, **49**, 14506–14519.
35 D. W. Chu, X. Zhao, B. X. Xiao, A. Libanori, Y. H. Zhou, L. C. Tan, H. Ma, H. Pang, X. Wang, Y. Jiang and J. Chen, *Chem. Eur. J.*, 2021, **27**, 8337–8343.
36 N. S. Neeraj, B. Mordina, A. K. Srivastava, K. Mukhopadhyay and N. E. Prasad, *Appl. Sur. Sci.*, 2019, **473**, 807–819.
37 Y. Zhang, C. R. Chang, X. D. Jia, Y. Cao, J. Yan, H. W. Luo, H. L. Gao, Y. Ru, H. X. Mei, A. Q. Zhang, K. Z. Gao and L. Z. Wang, *Inorg. Chem. Commun.*, 2020, **112**, 107697.
38 Y. C. Sun, X. W. Wang, W. C. Zhang and X. Wu, *CrystEngComm*, 2021, **23**, 7671–7678.
39 H. M. Zhao, Z. P. Zhang, C. G. Zhou and H. F. Zhang, *Appl. Surf. Sci.*, 2021, **541**, 48458.
40 H. Q. Liu, M. Z. Dai, D. P. Zhao, X. Wu and B. Wang, *ACS Appl. Energy Mater.*, 2020, **3**, 7004–7010.
41 C. V. V. M. Gopi, S. Sambasivam, K. V. G. Raghavendra, R. Vinodh, I. M. Obaidat and H. J. Kim, *J Energy Storage*, 2020, **30**, 101550.
42 P. X. Sun, N. Li, C. G. Wang, J. M. Yin, G. Zhao, P. Y. Hou and X. J. Xu, *J. Power Sources*, 2019, **427**, 56–61.
43 Y. X. Zhong, T. W. Liu, A. T. Zhang, L. Cui, X. P. Liu, R. K. Zheng and J. Q. Liu, *J. Alloys Compd.*, 2021, **850**, 156734.
44 P. Sharma, M. M. Sundaram, T. Watcharatharapong, D. Laird, H. Euchner and R. Ahuja, *ACS Appl. Mater. Interfaces*, 2020, **12**, 44815–44829.